On Solving the Momentum Equations of Dynamic Sea Ice Models with Implicit Solvers and the Elastic-Viscous-Plastic Technique

Martin Losch*, Sergey Danilov

Alfred-Wegener-Institut für Polar- und Meeresforschung, Postfach 120161, 27515 Bremerhaven, Germany

Abstract

Experiments with idealized geometry are used to compare model solutions of implicit VP- and explicit EVP-solvers in two very different ice-ocean codes: the regular-grid, finite-volume Massachusetts Institute of Technology general circulation model (MITgcm) and the Alfred Wegener Institute Finite Element Ocean Model (FEOM). It is demonstrated that for both codes the obtained solutions of implicit VP- and EVP-solvers can differ significantly, because the EVP solutions tend to have smaller ice viscosities ("weaker" ice). EVP solutions tend to converge only slowly to implicit VP solutions for very small sub-cycling time steps. Variable resolution in the unstructured-grid model FEOM also affects the solution as smaller grid cell size leads to smaller viscosity in EVP solutions. Models with implicit VP-solvers can block narrow straits under certain conditions, while EVP-models are found to always allow flow as a consequence of lower viscosities.

Key words: NUMERICAL SEA ICE MODELING, VISCOUS-PLASTIC RHEOLOGY, EVP, ICE STRESS

*Corresponding author

Email addresses: `Martin.Losch@awi.de` (Martin Losch), `Sergey.Danilov@awi.de` (Sergey Danilov)

Preprint submitted to Ocean Modelling *October 5, 2011*

1. Introduction

Modeling sea ice dynamics has reached a state of maturity that makes it impossible not to include dynamic sea ice models in new state-of-the-art climate models (earth system models, ESM). Sea ice models with a viscous-plastic (VP) constitutive relation are found to reproduce observed drift well in comparison with models that do not include shear and bulk viscosities (Kreyscher et al., 2000). But, because of very large viscosities in regions of nearly rigid ice, models with a VP-dynamics component (e.g., Hibler, 1979, Kreyscher et al., 2000) require implicit, iterative methods. Further, implicit VP solvers have to impose an upper limit on the viscosity in order to regularize the problem. Hence, these models have been found to be difficult and time consuming to solve in the context of coupled ice-ocean model systems (Hunke, 2001). To make things worse, many of these iterative methods only solve the linearized problem. The non-linear convergence is much more expensive and requires many so-called pseudo time steps (Lemieux and Tremblay, 2009, but see also Hibler 1979, Flato and Hibler 1992, Zhang and Hibler 1997).

In contrast, the elastic-viscous-plastic (EVP) formulation of the Hibler model (Hunke and Dukowicz, 2002), which is now used in many coupled ice-ocean (and earth system) models, exploits the fact that ice models need to reduce to VP dynamics only on wind forcing time scales (generally on the order of 6 hours or longer), whereas at shorter time scales the adjustment takes place by a numerically efficient wave mechanism. These elastic waves regularize the system and implicitly reduce large viscosities. As a consequence, the EVP scheme is fully explicit in time and allows much longer time steps than a time-explicit nonlinear VP-scheme. Hunke and Dukowicz (1997), Hunke and Zhang (1999), Hunke

(2001), and recently Bouillon et al. (2009) and Losch et al. (2010) show that the EVP scheme can be far more efficient than previous implicit VP-schemes, especially for parallel computers.

On the other hand, Hunke (2001) illustrated examples of residual elastic waves in regions of nearly rigid ice and at high resolution, depending on the choice of parameters in the EVP model. The remaining elastic waves look like noise when the prescribed subcycling time step is too large to resolve the elastic wave damping time scale. Hunke (2001) suggested a limiting scheme for such a case that, based on a stability analysis, limits the ice strength and thus the elastic wave amplitude (see Section 3 for more details).

The ever increasing horizontal resolution in today's ice-ocean models requires short time steps (1 hour and less) so that some of the issues raised by Hunke (2001) need to be revisited. In particular, the effects of linearization in the implicit treatment of the VP equation become decreasingly severe with decreasing model time step (Lemieux and Tremblay, 2009). Also, the convergence of the implicit solvers are expected to improve with decreasing time step as the state of the dynamics changes only slowly within one short time step. Hence, the starting point for iterative solvers is already much closer to the solution than in the traditional case of 12–24 hours time steps in Hibler (1979). Hutchings et al. (2004) draw upon recent developments in computational fluid dynamics to develop efficient discretization and solution schemes that are also strictly mass conserving, and there are promising efforts that implement efficient solver algorithms. For example, Lemieux et al. (2008) adapt a GMRES algorithm and later (Lemieux et al., 2010) Jacobian-free Newton-Krylov methods to improve efficiency and convergence of the linearized equations. With these developments, solving the VP dynamics with implicit methods remains attractive and implicit methods will probably co-exist with the EVP approach.

Eventually, both methods of stress parameterization lead to bulk and shear viscosities. These viscosities describe the behavior of the VP-fluid, so that modifying them in any way effectively changes the rheology of ice. In this sense VP-solvers with different maximum viscosities and also EVP solvers describe different physical systems in the rigid ice (high viscosity) regime although initially they are based on the same constitutive law. It is important to note that both VP and EVP equations only approximate the true rheology and neither can be expected to be exact. In fact, completely different approaches are currently pursued that are neither VP nor EVP, for example, elasto-brittle rheology (Girard et al., 2011) and discrete element models (Wilchinsky and Feltham, 2006, Wilchinsky et al., 2010), but until these will have matured climate models will use either VP or EVP models. Here we aim to illustrate that there are substantial differences between these models that affect the large scale distribution of sea ice and that are easily traced back to the different methods of regularizing the large viscosities of the original VP-rheology. We can not provide criteria for choosing one variant over the other variant, because that can only be achieved for specific cases and configurations with detailed and extensive comparisons between models and observations and with inverse methods, but we want to raise awareness for the different behavior of the different methods.

In this paper we demonstrate that limiting viscosities to regularize the numerical problem of solving for drift velocities can influence solutions, especially on unstructured meshes with variable resolution. Even on regular meshes the solutions are sensitive to the details of the rheology because the effective viscosity in EVP can become very low compared to that of the VP solution. We compare VP and EVP solution strategies and revisit the problem of noise and limiting ice strength in the EVP solution in two different and independent implementations: The sea ice component of the unstructured-grid Alfred Wegener Institute Finite Element Ocean Model (FEOM, Danilov et al., 2004, Timmermann et al., 2009) and that of the regular-grid, finite-volume Massachusetts Institute of Technology general circulation model (MITgcm Group, 2010) as described in Losch et al. (2010). For both models Hunke's (2001) EVP solver is available. In addition, for the MITgcm the line successive over relaxation (LSOR) method of Zhang and Hibler (1997) is implemented, and FEOM implements a variant of Hutchings et al. (2004)'s strength explicit algorithm.

The paper is organized as follows: Section 2 reviews the model equations and describes details of their implementation. In Section 3 we illustrate with numerical experiments how various limiting schemes within FEOM depend on the resolution in an idealized configuration similar to that of Hunke (2001). In a second set of experiments we use drifting ice in an idealized geometry at high resolution to demonstrate the effects of the limiting scheme and the convergence of EVP to the LSOR solution with the MITgcm (Section 4). Conclusions are drawn in the final section.

2. Model Description

The vertically averaged (i.e. two-dimensional) momentum equations (e.g., Hibler, 1979) for all sea ice models in this study are

$$m\frac{D\mathbf{u}}{Dt} = -mf\mathbf{k}\times\mathbf{u} + \boldsymbol{\tau}_{air} + \boldsymbol{\tau}_{\text{ocean}} - m\nabla\phi + \mathbf{F}, \tag{1}$$

where $\mathbf{u} = u\mathbf{i} + v\mathbf{j}$ is the ice velocity vector, m the ice mass per unit area, f the Coriolis parameter, and $\nabla\phi$ is the gradient (tilt) of the potential due to the sea surface height (due to ocean dynamics) beneath the ice. $\boldsymbol{\tau}_{\text{air}}$ and $\boldsymbol{\tau}_{\text{ocean}}$ are the wind and ice-ocean stresses, respectively. $\mathbf{F}$ is the internal force and $\mathbf{i}$, $\mathbf{j}$, and $\mathbf{k}$ are the unit vectors in the x, y, and z directions. Advection of sea ice momentum is neglected ($D/Dt \rightarrow \partial/\partial t$). The wind and ice-ocean stress terms are given by

$$\boldsymbol{\tau}_{\text{air}} = \rho_{\text{air}} C_{\text{air}} |\mathbf{U}_{\text{air}}| R_{\text{air}} \mathbf{U}_{\text{air}} \tag{2}$$

$$\boldsymbol{\tau}_{\text{ocean}} = \rho_{\text{ocean}} C_{\text{ocean}} |\mathbf{U}_{\text{ocean}} - \mathbf{u}| R_{\text{ocean}} (\mathbf{U}_{\text{ocean}} - \mathbf{u}), \tag{3}$$

where $\mathbf{U}_{\text{air/ocean}}$ are the surface winds of the atmosphere and surface currents of the ocean, respectively. $C_{\text{air/ocean}}$ are air and ocean drag coefficients, and $\rho_{\text{air/ocean}}$ constant reference densities for air and sea water. Here, their values are set to $\rho_{\text{air}} = 1.3\,\text{kg}\,\text{m}^-3$ and $\rho_{\text{ocean}} = 1000\,\text{kg}\,\text{m}^-3$. $R_{\text{air/ocean}}$ are rotation matrices that act on the wind/current vectors to parameterize unresolved Ekman boundary layers. Here, the rotation angle θ is generally zero ($R_{\text{air/ocean}} = 1$), except where noted otherwise. The internal force $\mathbf{F} = \nabla \cdot \sigma$ is given by the divergence of the internal stress tensor σ_{ij}. Note that in all expermients presented here the ocean models are stationary and do not react to changes in the ice cover. In all of these "off-line" simulations the ocean currents $\mathbf{U}_{\text{ocean}}$ are prescribed and the sea surface is assumed to be flat ($\nabla\phi = 0$).

For an isotropic system this stress tensor σ_{ij} can be related to the ice strain rate and strength by a nonlinear viscous-plastic (VP) constitutive law (Hibler, 1979, Zhang and Hibler, 1997). Hunke and Dukowicz (1997) introduced an elastic contribution to the strain rate in order to regularize the VP constitutive law in such a way that the resulting elastic-viscous-plastic (EVP) and VP models are identical in steady state ($\frac{\partial\sigma}{\partial t} \rightarrow 0$),

$$\frac{1}{E}\frac{\partial\sigma_{ij}}{\partial t} + \frac{1}{2\eta}\sigma_{ij} + \frac{\eta-\zeta}{4\zeta\eta}\sigma_{kk}\delta_{ij} + \frac{P}{4\zeta}\delta_{ij} = \dot{\epsilon}_{ij}, \tag{4}$$

with the modulus of elasticity E, the bulk and shear viscosities ζ and η and the Kronecker symbol δ_{ij} ($\delta_{ij} = 1$ for $i = j$ and 0 otherwise). The ice strain rate is given by

$$\dot{\epsilon}_{ij} = \frac{1}{2}\left(\frac{\partial u_i}{\partial x_j} + \frac{\partial u_j}{\partial x_i}\right). \tag{5}$$

The pressure term P is computed from the ice thickness characteristics and the strain rate, according to the pressure replacement method of Hibler and Ip (1995, see below). The (maximum) ice pressure $P_{\max}$, a measure of ice strength, is parameterized by ice thickness h and compactness (concentration) c as:

$$P_{\max} = P^{*} c\, h\, \exp\{-C^{*} \cdot (1-c)\}, \tag{6}$$

with the tuning constants $P^{*} = 27,500\,\mathrm{N\,m^{-2}}$ and $C^{*} = 20$. Following Hibler (1979), the nonlinear bulk and shear viscosities η and ζ are functions of ice strain rate invariants and ice strength such that the principal components of the stress lie on an elliptic yield curve with the ratio of major to minor axis e equal to 2; they are given by

$$\zeta = \frac{P_{\max}}{2\max(\Delta, \Delta_{\min})} \tag{7}$$

$$\eta = \frac{\zeta}{e^2} \tag{8}$$

with the abbreviation

$$\Delta = \left[\left(\dot{\epsilon}_{11}^2 + \dot{\epsilon}_{22}^2\right)(1+e^{-2}) + 4e^{-2}\dot{\epsilon}_{12}^2 + 2\dot{\epsilon}_{11}\dot{\epsilon}_{22}(1-e^{-2})\right]^{\frac{1}{2}}. \tag{9}$$

The viscosities are bounded from above by imposing a minimum $\Delta_{\min} = 10^{-11}\,\mathrm{s^{-1}}$ to avoid divisions by small numbers. For the implicit VP solvers, this limit is raised to $2 \times 10^{-9}\,\mathrm{s}^{-1}$ to give lower viscosities and faster convergences of the iterative solvers. For stress tensor computation according to Eq. (4), the replacement pressure $P = 2\,\Delta\zeta$ (Hibler and Ip, 1995) is used.

The original VP-model is obtained by setting $\frac{\partial \sigma_{ij}}{\partial t} = 0$ in (4). In the MITgcm implementation the resulting momentum equations are integrated with the semi-implicit line successive over relaxation (LSOR)-solver of Zhang and Hibler (1997). This method allows a long model time step Δt that is, in our case, limited only by the explicit treatment of the Coriolis term. The solver is called once for a Eulerian time step and then a second time with updated viscosities for a modified Eulerian time step (Zhang and Hibler, 1997). In addition further modified Eulerian time steps can be made to converge in a non-linear sense similar to Lemieux and Tremblay (2009). This procedure corresponds to the pseudo-time steps of Zhang and Hibler (1997). Following Lemieux and Tremblay (2009), we will call each call of the LSOR solver an outer loop (OL) iteration.

The VP implementation of FEOM follows the approach of the explicit strength algorithm of Hutchings et al. (2004), with time stepping organized similar to that of Zhang and Hibler (1997). The block Jacobi preconditioned BICGstab algorithm of PETSc (Balay et al., 2002) is used to solve matrix problems on the unstructured grid of FEOM.

The EVP-model, on the other hand, uses an explicit time stepping scheme with a short sub-cycling time step $\Delta t_e \ll \Delta t$. According to the recommendation of Hunke and Dukowicz (1997), the EVP-model is stepped forward in time 120 times within the ocean model time step. At each sub-cycling time step, the visocities ζ and η are updated following Hunke (2001). The elastic modulus E is redefined in terms of a damping time scale $T = E_0 \Delta t$ for elastic waves

$$E = \frac{\zeta}{T} \tag{10}$$

with the tunable parameter $E_0 < 1$ and the external (long) model time step Δt. We use 0.36 as Hunke (2001). For a time step of $\Delta t = 1\,\mathrm{h}$, this amounts to $T = 1296\,\mathrm{s}$. In regions of almost rigid ice, this choice of parameters can lead to noisy solutions when the elastic time scale is not resolved properly. Hunke (2001) suggests an additional constraint on the ice strength that is derived from a numerical stability criterion:

$$\frac{P}{\max(\Delta, \Delta_{min})} < \frac{C\, T\, a}{(\Delta t_e)^2}, \tag{11}$$

with the grid cell area a and a tuning parameter C. If not noted otherwise, we use $C = 615\,\mathrm{kg\,m^{-2}}$ according to Hunke (2001). To our knowledge, relation (11) was never employed in realistic climate simulations. Although it is a useful tool for understanding and eliminating potential issues associated with elastic waves and noise in viscosities and ice velocity divergence, it can not be recommended for general use in climate runs (E. Hunke, pers. com. 2011). We illustrate this statement with some examples below.

The spatial discretization of the MITgcm models is outlined in the appendix of Losch et al. (2010). The MITgcm use a finite-volume discretization on an Arakawa-C grid with staggered velocity and center (thickness) points. All metric terms are included (although on the cartesian grids of this paper, they are zero). The derivates in the strain rates $\dot{\epsilon}_{ij}$ are approximated by central differences. Averaging is required between center points and corner points.

The FEOM uses a discretization with linear basis functions on a triangular mesh. Ice velocities, thickness and concentration are co-located on the grid nodes (similar to an Arakawa-A grid). Strain rates, and components of the stress tensor are then naturally constant on triangles. The finite-element method solves the weak form of the equations, so that the divergence of stress is integrated by parts and no explicit stress differentiation is required.

3. Effects of resolution and limiting viscosity in rigid ice conditions

In this section we present examples of the effects of limiting the viscosity ζ in combination with a spatially variable mesh. Hunke (2001) introduced the limiting scheme (11) in order to suppress noise in the EVP solution, so we start by revisiting the experimental configuration of Hunke (2001). This L_x=1264 by L_y =1264 km square box configuration with 80 by 80 grid points (16 km resolution) contains a few islands (Figure 1, see also Hunke, 2001). Atmospheric wind and oceanic surface forcing are prescribed as

$$U_{\mathrm{air}} = \left\{5 + (\sin(2\pi t/\Theta) - 3)\sin(2\pi x/L_x)\sin(\pi y/L_y)\right\}\ \mathrm{m\,s^{-1}}, \tag{12}$$

$$V_{\mathrm{air}} = \left\{5 + (\sin(2\pi t/\Theta) - 3)\sin(2\pi y/L_y)\sin(\pi x/L_x)\right\}\ \mathrm{m\,s^{-1}}, \tag{13}$$

and

$$U_{\mathrm{ocean}} = \quad 0.1\,\mathrm{m\,s^{-1}}\ (2y - L_y)/L_y \tag{14}$$

$$V_{\mathrm{ocean}} = -0.1\,\mathrm{m\,s^{-1}}\ (2x - L_x)/L_x \tag{15}$$

where $\Theta = 4$ days. The rotation angle for the ice-ocean drag is 25°. The origin of the coordinate system $(x, y) = (0, 0)$ is at the south-west corner of the domain. The drag coefficients are $C_{\mathrm{air}} = 5 \times 10^{-4}$ (this value is very small but provides the best agreement with Hunke's choice) and $C_{\mathrm{ocean}} = 5.5 \times 10^{-3}$. The initial ice thickness increases linearly from 0 to 2 m and the initial ice compactness from 0 to 1 from left to right. All thermodynamic processes in the ice and the advection of ice thickness and compactness are turned off, as in the original experiments of Hunke (2001), so that the ice distribution does not change, either.

3.1. Reduced viscosities on a regular grid

We repeat Hunke's calculations (i.e., the domain contains islands and the ice thickness and compactness do not change in time) with the sea ice component of the MITgcm (MITgcm Group, 2010, Losch et al., 2010). Figure 1 (compare to Fig. 4 in Hunke, 2001) shows the ice velocity field, its divergence, and the bulk viscosity ζ after 9 days of integration for three cases: One solution with Zhang and Hibler (1997)'s LSOR solver (with a solver accuracy, i.e. target residual of initial residual, of 10^{-4}) and two solutions with the EVP solver, one without extra limiting and one where Hunke's limiting scheme has been implemented (Eq. (11)). This scheme limits ice strength and viscosities as a function of damping time scale, resolution and EVP-time step, in effect allowing the elastic waves to damp out more quickly (Hunke, 2001). All solutions are obtained on an Arakawa C-grid.

In the far right ("east") side of the domain the ice concentration is close to one and the ice is nearly rigid. The applied wind tends to push ice toward the upper right corner. Because the highly compact ice is confined by the boundary, it resists any further compression and exhibits little motion in the rigid region near the eastern boundary of the domain. The LSOR solution (left column in Figure 1) allows high viscosities in the rigid region suppressing nearly all flow. Hunke (2001)'s limiting scheme for the EVP solution (right column) clearly suppresses the noise present in $\nabla\cdot\mathbf{u}$ and ζ in the unlimited case (middle column); it does so at the cost of reduced viscosities. Note that the viscosities in the EVP case without limiting are already reduced with respect to the LSOR solution. These reduced

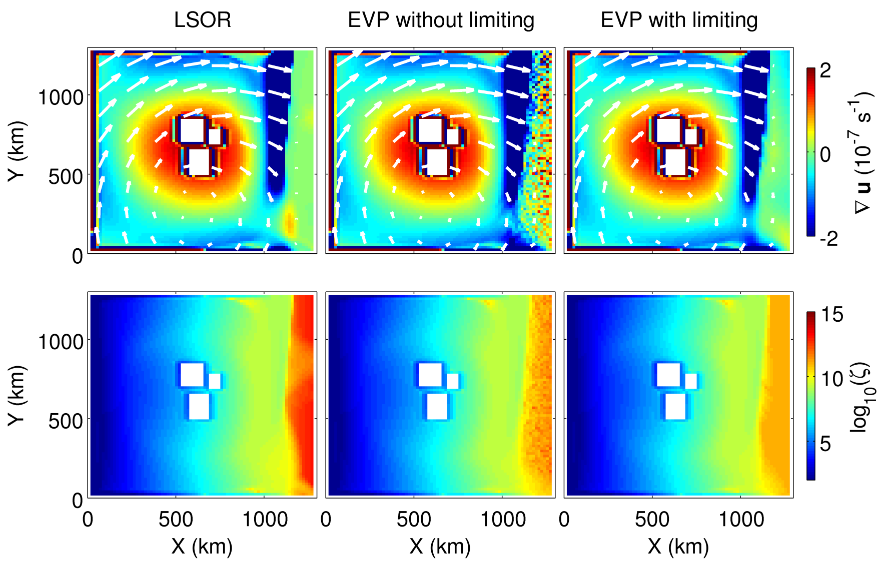

Figure 1: Ice flow (white arrows) and divergence (top row, in $10^{-7}\,\mathrm{s}^{-1}$ negative values imply convergent flow) and bulk viscosities (bottom row, in $\mathrm{N\,s\,m}^{-1}$, logarithmic scale) of three experiments with Hunke (2001)'s test case: implicit solver LSOR (left), EVP (middle), and EVP with limiting as described in Hunke (2001) (right).

viscosities lead to small but finite ice drift velocities in the right hand side ("east") of the domain where ice is very thick and rigid (not visible in Figure 1 because of the scale of the arrows). These velocities in turn can, in the limit of nearly rigid regimes, determine whether ice can block a narrow passage or not (see also Section 4).

So far the LSOR solutions were obtained with two Eulerian steps. Lemieux and Tremblay (2009) showed that a complete convergence to the non-linear solution may require many more OL iterations with updated viscosities. Figure 2 shows the viscosity of LSOR solutions with 10 OL-iterations (top left hand cor-

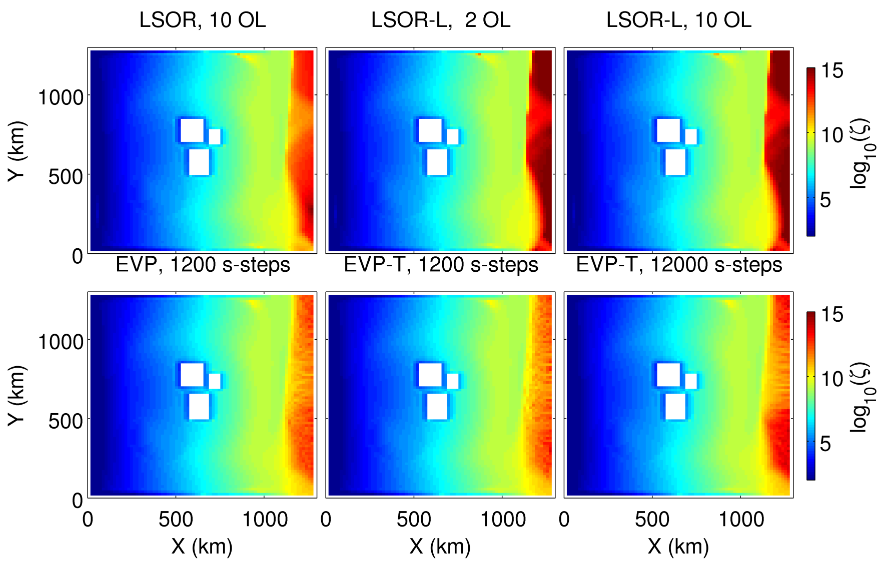

Figure 2: Bulk viscosities (in $\mathrm{N\,s\,m^{-1}}$) for various cases. Top row, from left to right: LSOR with 10 outer loop (OL) iterations, 2 OL-iterations with small $\Delta_{\min} = 0.5 \times 10^{-20}\,\mathrm{s}^{-1}$, 10 OL-iterations also with small $\Delta_{\min}$. Bottom row, from left to right: EVP with 1200 sub-cycles and $T = 1296\,\mathrm{s}$, with 1200 sub-cycles and $T = 129.6\,\mathrm{s}$, and with 12000 sub-cycles and $T = 12.96\,\mathrm{s}$. Note the logarithmic color scale.

ner). In general, more OL-iterations lead to higher viscosities along the right-hand boundary of the domain, where the ice is rigid, making the difference to the EVP solutions even larger. To illustrate the limiting of the viscosities, we show a case with $\Delta_{\min} = 0.5 \times 10^{-20}\,\mathrm{s}^{-1}$, so with a more than 10 orders of magnitude larger maximum ζ, with 2 and with 10 OL-iterations (Figure 2, top row, middle and right hand panel). In this case the much larger viscosities do not become much larger with more OL-iterations.

A naive way to make EVP solutions converge to VP solutions ($\frac{\partial\sigma}{\partial t} \rightarrow 0$) is to reduce the damping time scale T and the sub-cycling time step Δt_e. Reducing T makes the system relax faster to the VP state, but requires also shorter time steps to resolve T. Reducing Δt_e for fixed T improves the resolution of the damping scale. We show 3 cases with reduced $\Delta t_e = 3\,\mathrm{s}$, reduced $T = 129.6\,\mathrm{s}$ with constant $\Delta t_e/T$, reduced T and further reduced Δt_e (bottom row of Figure 2, left to right). Reducing Δt_e reduces the noise in the velocity fields and also increases the viscosities. Reducing T has little noticeable effect.

In summary, EVP solutions have generally lower viscosities than LSOR solutions. Increasing the accuracy of the solvers has a stronger effect in the LSOR solution while the EVP solutions are affected to a much smaller extent.

3.2. Effects of variable resolution

After repeating the experiments of (Hunke, 2001), we use the sea ice component of the unstructured-grid model FEOM to go further and illustrate the effect of variable resolution on limiting ζ. Two different unstructured meshes are used to discretize the domain. In the first one (Mesh 1) the resolution increases smoothly from 40 km at the southern boundary to less than 10 km at the northern boundary; the second mesh (Mesh 2) is the first one inverted, so that now the coarse resolution is in the north. The islands are removed to ensure that the domain is not changed with the mesh transformation. The meshes provide approximately the same mean resolution as in Hunke (2001). The patterns of Figure 1 are reproduced in both cases (not shown). In order to emphasize the influence of the resolution the simulations are repeated, but now ice advection by the drift velocities is enabled with a finite-element flux-corrected transport scheme (FEM-FCT, Löhner et al., 1987). Note that the effects discussed below are not connected to the type of mesh. They are not found on unstructured meshes with uniform resolution (not shown).

The wind and ocean circulation drive the ice to become very thick and rigid in the upper right hand corner of the domain. As the limiting scheme of Hunke (2001) depends on the grid cell area, we expect a larger effect for the first mesh with high resolution in the upper half of the domain. The model is integrated for two months with three different solver schemes on each mesh: the strength explicit viscous-plastic algorithm of Hutchings et al. (2004), the EVP scheme without limiting, and the EVP scheme with a limiting constant of $C = 615\,\mathrm{kg/m^2}$ (as recommended by Hunke, 2001). The runs will be referred to as VP, EVPNL, and EVPL, respectively. The drag coefficient is $C_{\mathrm{air}} = 22.5 \times 10^{-4}$ in all cases.

The left column of Figure 3 shows the effective thickness (in meters) of the VP runs after 2 months of integration. As expected, the wind drives the ice into the upper right hand corner where it piles up. Although the runs EVPL and EVPNL develop similar ice patterns, their ice distribution differs from the VP case (Figure 3, middle and right panels of the top row). This difference is already large (order 2 m) for the EVPNL case, but for the EVPL case with limiting the difference to the VP result has the same order of magnitude as the VP ice thickness itself.

The bulk viscosities, shown in Figure 4 for the simulations on Mesh 1, are smaller than for VP in both the EVPNL and EVPL cases, in particular in the upper right corner where the resolution is high. Thus, these cases allow slow ice motion towards the corner that piles up the ice. Because of the extra limiting, the effect is much larger in EVPL, as expected. In the EVPNL run not all variables are smooth (not shown, but similar to Figure 1), but there is no apparent noise in ice volume or compactness fields.

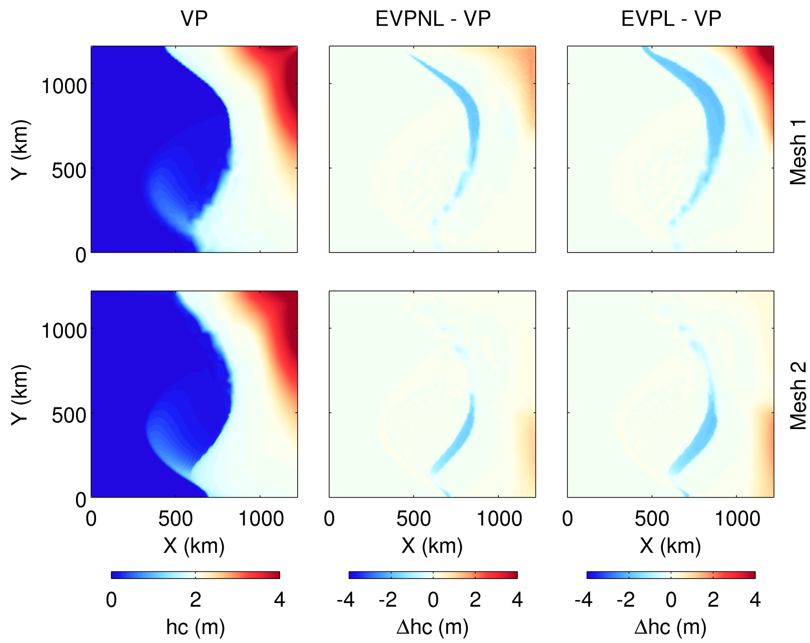

Figure 3: Effective ice thickness (in meters) after 2 months of integration for the three simulations: VP (left), difference EVPNL-VP (middle), and difference EVPL-VP (right) on Mesh 1 (top row) and Mesh 2 (bottom row).

For Mesh 2 with low resolution in the north (Figure 3, bottom row), the area with limited viscosity in the EVP simulations is much smaller (not shown). Further, even in the case EVPL, the viscosity limiting is not as strong as on Mesh 1 and allows higher viscosity values because the resolution is coarse where the ice is thick and the limiting scheme applies. As a result, the differences between the ice volume fields of the VP, EVPL and EVPNL simulations are much smaller than for Mesh 1.

In summary, using an EVP implementation on meshes with variable resolution requires care, because the limiting mechanism of EVP can lead to large deviations of the ice thickness from the viscous-plastic solution in areas of high resolution.

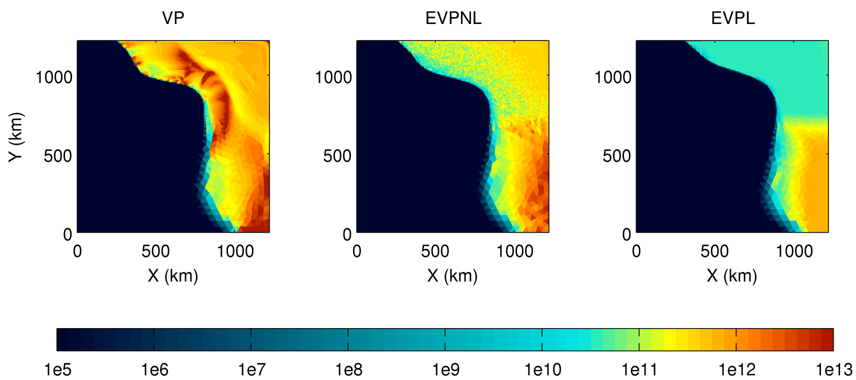

Figure 4: Bulk viscosity ζ (in in $\mathrm{N\,s\,m^{-1}}$) after 2 months of integration for the three FEOM simulations on Mesh 1: VP (left), EVPNL (middle), and EVPL (right).

While these effects are large on grids with variable resolution, they are also present on more common grids with constant resolution. This last point is also addressed in the next section.

4. Effects of reduced viscosity in a channel with drifting ice

In a second set of experiments we give another example of how regularizing the viscosity can alter the solution. At the same time we demonstrate how, for short sub-cycling time steps, the EVP solution tends towards the solution obtained with the LSOR-solver.

4.1. High drift velocities

For these experiments we employ the sea ice component of the MITgcm in an idealized geometry. In a re-entrant channel, 1000 km long and 500 km wide

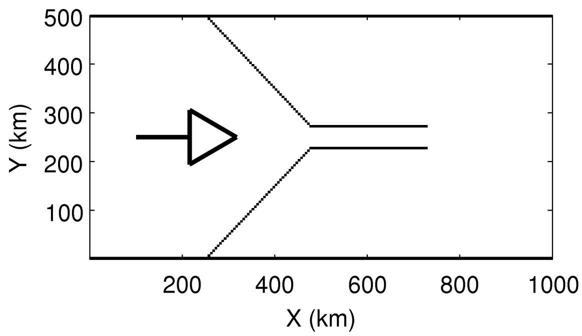

Figure 5: Geometry of re-entrant channel with funnel. The arrow indicates the direction of the forcing and of the ice drift.

on a non-rotating plane, converging walls form a symmetric funnel and a narrow strait of 40 km width. The exit of this channel is approximately at $x = 750$ km, so that further to the right the ice flow is unconstrained by lateral walls until it re-enters the channel from the left and encounters the funnel again (Figure 5). The horizontal resolution is 5 km throughout the domain making the narrow strait 8 grid points wide. While this is probably at the limit of resolving the strait, grids with such straits or opening are not unusual in climate modeling with regular grids. For example, Fieg et al. (2010) use a regional model with a rotated (1/12)th degree grid. With this resolution of approximately 9 km, the narrow passages such as the Nares Strait are still represented by only a few grid cells.

The ice model is initialized with a completely closed ice cover ($c = 1$) of uniform thickness $h = 0.5$ m and driven by stress that corresponds to a uniform, constant along-channel eastward ocean current of $25\,\mathrm{cm\,s^{-1}}$. (This is nearly the same as prescribing uniform wind velocity of approximately $23\,\mathrm{m\,s^{-1}}$. We chose ocean velocities because it is technically simpler to prescribe them in our code.)

All other ice-ocean-atmosphere interactions are turned off, in particular there is no feedback of ice dynamics on the ocean current. All thermodynamic processes are turned off so that ice thickness variations are only caused by convergent or divergent ice flow. Ice volume (effective thickness) and concentration are advected with a third-order scheme with a flux limiter (Hundsdorfer and Trompert, 1994) to avoid undershoots. This scheme is unconditionally stable and does not require additional diffusion. In the case of converging ice with ice concentrations > 1 a simple ridging scheme is used to reset the concentration to 1 (Hibler, 1979). The model is integrated for 10 years with a time step of 1 h until a steady state is reached. Note, that steady state means that effectively the solutions are converged also in a non-linear sense, so that increasing the number of OL-iterations for the LSOR solver does not change the solution (not shown). In general, the ice-ocean stress pushes the ice cover eastwards, where it converges in the funnel. After a short time the region in the lee of the funnel is ice-free because ice can not penetrate the funnel walls. In the narrow channel the ice moves quickly (nearly free drift) and leaves the channel as narrow band.

Figure 6 compares the dynamic fields ice concentration c, effective thickness $h_{\text{eff}} = h \cdot c$, and velocities (u, v) for three different cases at steady state (after 10 years of integration):

B-LSR: LSOR solver on a B-grid;

C-LSR: LSOR solver on a C-grid;

C-EVP: EVP solver on a C-grid; there are three cases $\Delta t_e = 30\,\text{s}$, $\Delta t_e = 3\,\text{s}$, and $\Delta t_e = 0.3\,\text{s}$.

All experiments presented here implement no-slip boundary conditions. At a first glance, the solutions look similar. This is encouraging as the details of discretization and numerics should not affect the solutions to first order.

A closer look reveals interesting differences especially in the narrow channel (Figure 7). Both LSOR solutions have a similar distribution of ice (≈ 2 m) in the narrow channel with the B-grid solution being slightly thicker, but the concentration at the boundaries in the C-grid solution is very low. Also the flow speeds are different. The zonal velocity is nearly the free drift velocity (= ocean velocity) of $25\,\mathrm{cm\,s^{-1}}$ for the C-grid solution. For the B-grid solution it is just above $20\,\mathrm{cm\,s^{-1}}$ and the ice accelerates to $25\,\mathrm{cm\,s^{-1}}$ only after it exits the channel. Since the effective thickness and concentration determine the ice strength P in Eq. (6), ice strength and thus the bulk and shear viscosities along the boundaries are larger in the B-grid case leading to more horizontal friction. With more horizontal friction the no-slip boundary conditions in the B-grid case are more effective in reducing the flow within the narrow channel, than in the C-grid case. The evolution of different steady-state balances between ice-ocean stress and internal stress divergence in the B- and C-grid case is probably determined by details of the boundary conditions at the entrance of the narrow channel that lead to different distributions of thickness, concentration and hence ice strength P.

The difference between LSOR and EVP solutions is largest in the effective thickness and meridional velocity fields. The EVP fields are a little noisy. This noise has been addressed by Hunke (2001), see also the previous section (Figure 1). For the EVP experiments we use 120, 1200, and 12000 sub-cycling steps, corresponding to sub-cycling time steps of $\Delta t_e = 30, 3,$ and 0.3 s. Results are also shown in Figure 6 and Figure 7. Thicker ice with slightly higher concentration (dash-dotted lines) is advected through the narrow channel at lower speeds than

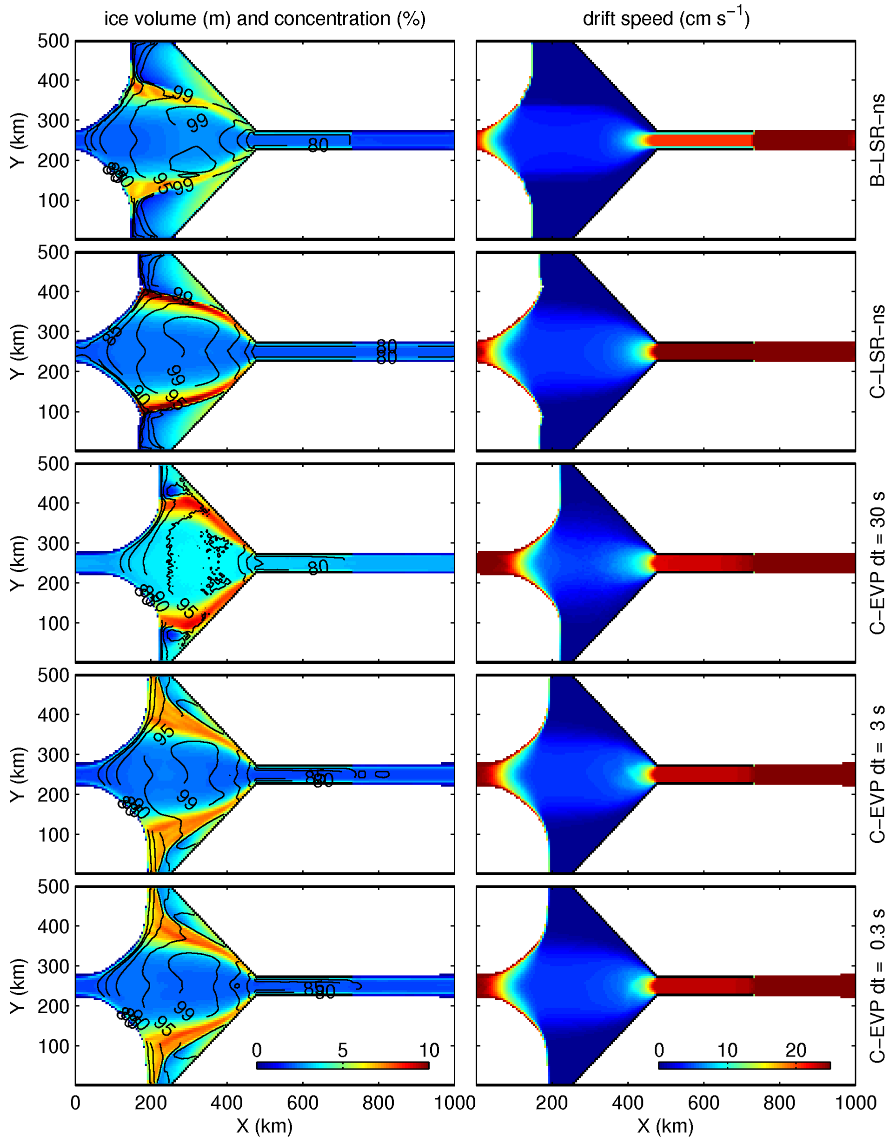

Figure 6: Ice concentration (80%, 85%, 90%, 95%, and 99% contour lines), effective thickness (color, in m), and ice drift speed (cm s^{-1}) for 5 different numerical solutions. Top to bottom: B-LSR, C-LSR, C-EVP with Δt_e = 30 s, 3 s and 0.3 s.

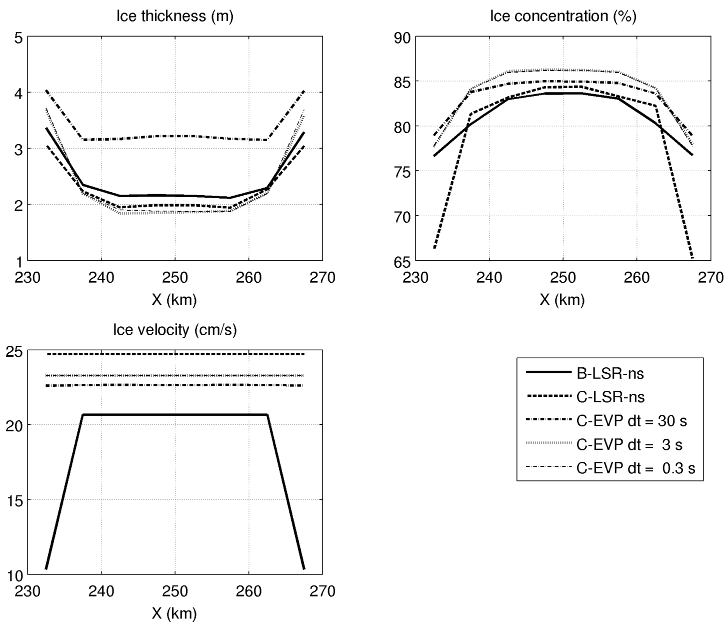

Figure 7: Effective thickness (m), ice concentration (%) ice velocity (cm s^{-1}) along a section across the narrow channel near X = 500 km for 5 different numerical solutions.

in the C-LSOR solution (approximately 22.5 cm s^{-1}). The C-EVP solution (dash-dotted lines) has thicker ice at slightly higher concentration in the narrow channel. As a consequence the drift speed is lower than in the C-LSR solution (approximately 22.5 cm s^{-1}). More sub-cycling time steps (smaller Δt_e) tend to reduce the ice thickness and increase the ice velocity, thus converge to the C-LSR solution, but ice concentration tends to increase away from the C-LSR solution. The EVP solution tends to converge with the increasing number of sub-cycling steps (decreasing Δt_e). $\Delta t_e = 3$ s appears to be sufficient to resolve the elastic time scale: the noise in the velocity has nearly vanished and reducing Δt_e to 3 s has very little effect.

For completeness we mention that we chose a low solver accuracy (target residual relative to initial residual) of 10^{-4} for the LSOR solution. Experiments with higher accuracies (smaller target residuals) take much longer to integrate but give only slightly different results (not shown).

The limiting scheme of Eq. (11) reduces the ice strength and viscosities so much that all ice can be pushed through the channel where it forms a stream of very thick ice (order 9 m, not shown). This strong reaction is not likely to occur in a realistic geometry with highly fluctuating forcing, but our example re-iterates that different limiting schemes can lead to dramatically different results. For this reason we recommend that the EVP pressure limiting scheme (Eq. 11) be used only for testing purposes, but not in reaslistic sea ice simulations.

4.2. Low drift velocities

So far, the differences between B- and C-grid, LSOR and EVP solver (without extra limiting) have been small. Now we present an example where the B- and C-grid LSOR solver yields a solution with a blocked channel, while the EVP solutions allow flow through the channel. Stopping flow and stable ice bridges or arches are observed and they have been simulated successfully on short time scales (Hibler et al., 2006, Dumont et al., 2009), but it is not clear *a-priori* that implementations of VP-rheology allow blocked flow, because imposing maximum viscosities allow finite drift velocities ("creep") in nearly rigid regimes that will eventually break up any ice block. Figure 8 shows Hovmöller-diagrams along $Y = 1800$ km and Figure 9 shows snapshots at day 1795 of experiments where the driving ocean velocities have been reduced to $10\,\mathrm{cm\,s^{-1}}$. All other configuration parameters are the same as before.

In the B-LSR solution the ice drift nearly comes to a halt within the narrow channel of 40 km width (8 grid cells), marked by the vertical (magenta) lines. A

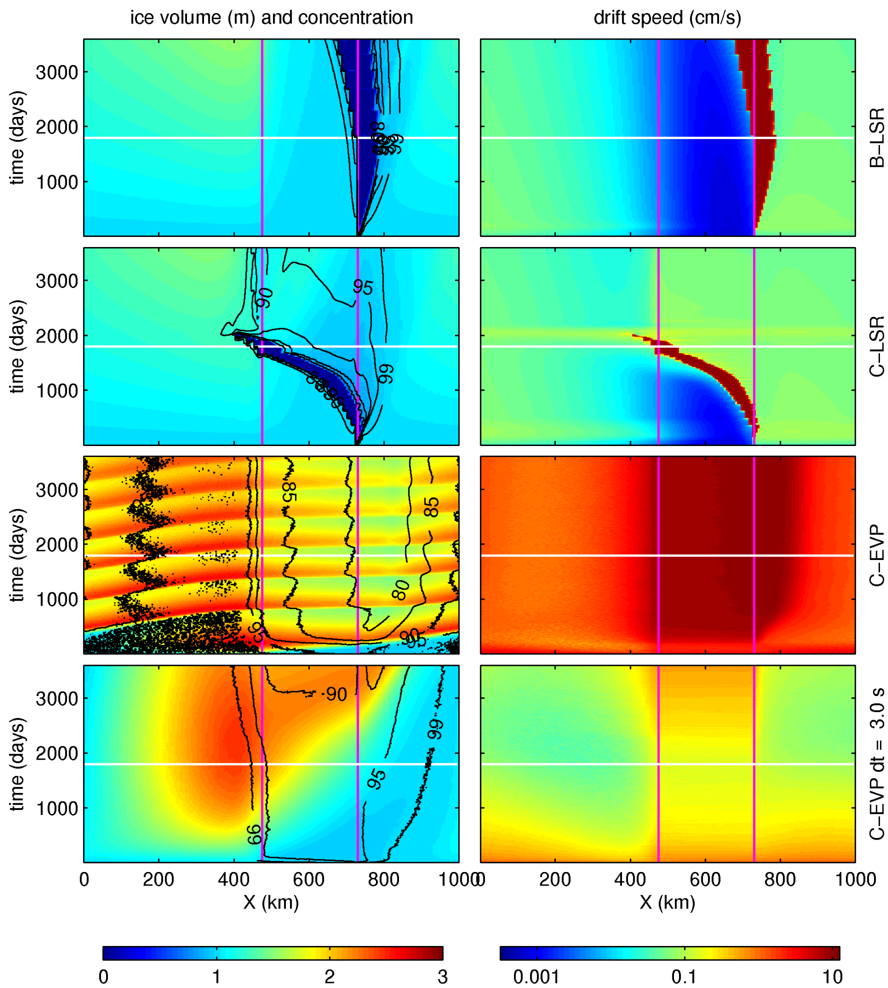

Figure 8: Hovmöller-diagrams of ice concentration (80%, 85%, 90%, 95%, and 99% contour lines), effective thickness (color, in m), and ice drift speed (cm s^{-1}, note the logarithmic color scale) for 3 different numerical solutions. Top to bottom: B-LSR, C-LSR, C-EVP with $\Delta t_e = 30$ s and 3 s. The vertical magenta lines mark the location of the narrow channel. The white horizontal line marks the time (day 1795) of the snapshot shown in Figure 9.

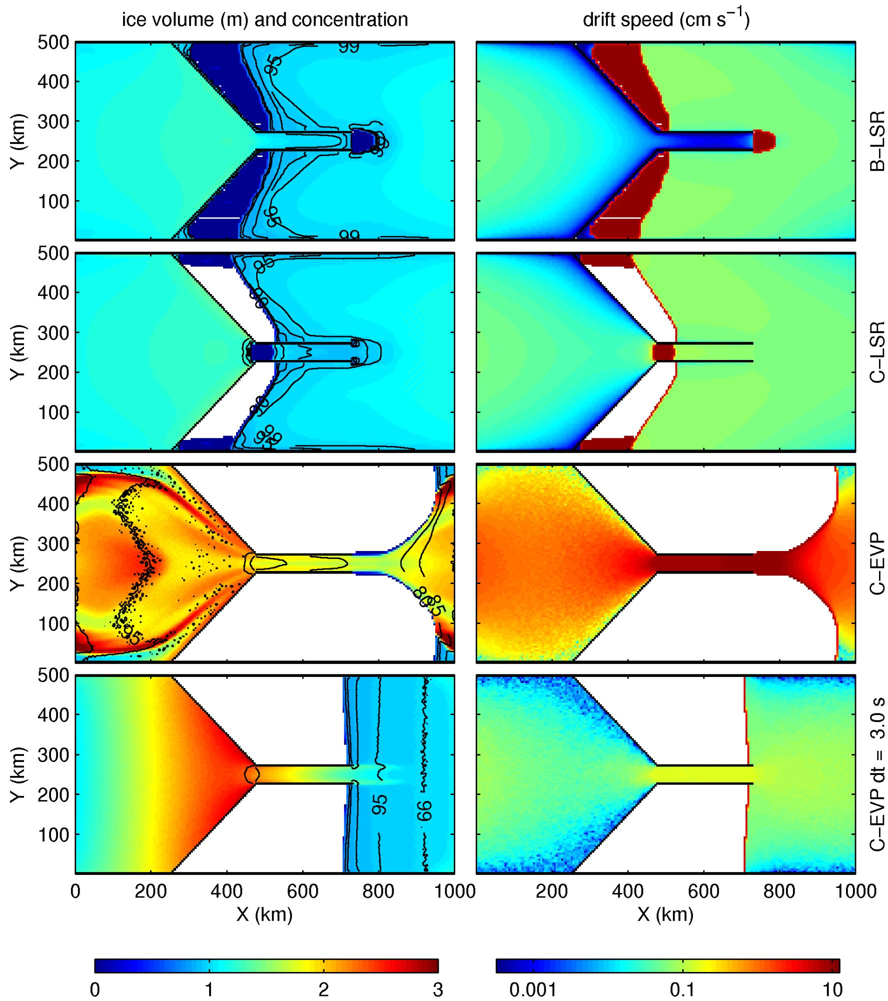

Figure 9: Ice concentration (80%, 85%, 90%, 95%, and 99% contour lines), effective thickness (color, in m), and ice drift speed (cm s^{-1}, note the logarithmic color scale) for 3 different numerical solutions after 1795 days. Top to bottom: B-LSR, C-LSR, C-EVP with $\Delta t_e = 30\,\mathrm{s}$, and 3 s.

lead with very low ice concentration ($< 1\%$) forms in the lee of the channel exit, as ice is moved away but is not resupplied from the channel. With time, this lead moves slowly into the channel. The C-LSR solution exhibits a similar behavior, except that the lead moves into and through the channel more quickly. At the time of the snapshot in Figure 9, marked by the horizontal white line in Figure 8, the lead has reached the upstream end of the channel and the ice forms an arch. When the lead emerges from the channel it dissolves and the blocking event is over.

For the C-EVP solutions the drift within the channel is never reduced, but rather accelerated compared to flow outside the channel. The ice distribution is also dramatically different from the LSOR solutions (see also the snapshot in Figure 9) and the sea-ice appears to behave like a viscous Newtonian fluid. The apparent periodicity stems from the initial pulse of ice that moves from the lee of the funnel walls into the main ice stream. This ice thickness maximum circulates in the re-entrant channel to appear as a false oscillation. Similar false oscillation patterns are also seen in LSOR solutions under different (stronger) forcing and are not an artefact of the EVP solution. It is interesting to note that increasing the number of sub-cycles in EVP changes the solution towards the LSOR solutions (bottom rows of Figures 8 and 9). This tendency continues for even more sub-cycling time steps (not shown), but we did not manage to generate an EVP-simulation with the parameters of this experiment where the flow comes to a near-halt as in the LSOR solutions. Dumont et al. (2009) report arching or stable ice bridges in a similar idealized configuration with an EVP-model for values of the eccentricity $e < 2$ (see Eq. (8)); reducing e means increasing the lateral shear, and thus the cohesion. Dumont et al. evaluate their criteria for a stable ice bridge after the first 30 days of their simulations. Our example is extreme, as we run the model for 10 years and evaluate the overall development. Ice bridges that are formed within the first days of the simulation are not considered nor modifications of the eccentricity, so that we can not claim that there will not be any ice bridges in our EVP-solutions.

As a side remark, we also ran both LSOR and EVP solvers with free-slip boundary conditions. Free-slip boundary conditions may not be relevant to sea-ice modeling, but it is still interesting to note that the LSOR solution with free-slip boundary conditions, as expected, does not lead to stopping flow, but looks similar to the C-EVP solution with $\Delta t_e = 3\,\mathrm{s}$ (not shown). The free-slip conditions do not have a noticeable effect on the EVP solution. Further, from (Losch et al., 2010, their Fig. 4) we expected that changing the advection scheme has an impact on the solution in narrow channels, but we found that changing the advection scheme from 3rd order to 2nd order hardly affects the solutions in the experiments of this section.

5. Discussion and Conclusion

Solving the equations of motion for thick sea ice is not trivial because large internal stresses give rise to numerical challenges. The EVP approach has been shown previously to be more efficient (Hunke and Dukowicz, 1997, Hunke and Zhang, 1999, Bouillon et al., 2009, Losch et al., 2010) and more accurate (Hunke and Zhang, 1999, Hunke, 2001) in modeling sea ice dynamics than implicit methods. However, EVP solvers implement different constitutive equations than VP solvers and our simple experiments demonstrate that as a consequence the solutions are also different. In particular:

- The EVP code is stable despite the noise that appears if the internal time step is insufficiently small, but we found only very slow and incomplete convergence to the viscous-plastic rheology as approximated by our VP solvers.

- Reaching convergence to nearly VP solutions requires very small time steps so that the EVP code loses its efficiency.

- Specific cases where LSOR lead to a blocked flow can not be recovered with EVP ice-dynamics. While blocking regimes and arching ice are observed, it is not clear to us whether the behavior of the LSOR solution represents the VP-rheology, or whether it is the consequence of numerical implementation details.

The limiting scheme of Hunke (2001) was designed to alleviate a noise problem in EVP solvers. (Later, stability was recovered in Hunke's model in a physical way by modifying the ridging scheme (Lipscomb et al., 2007).) Although this scheme—to our knowledge—has never been used in realistic applications, we note, that it can lead to solutions that deviate from expectations. The most likely reason is that this scheme reduces the ice viscosities dramatically below the VP values. Further, there are resolution-induced effects on computational grids with variable resolution that are larger with EVP (and particularly with the limiting scheme) than with VP solvers. We emphasize that none of the above points can be evidence that VP solutions are superior to EVP solutions. In fact, the VP-rheology is an approximation to the true rheology and should be tested against observations as much as any other approximation such as EVP (an example, where EVP gives more accurate results, can be found in Hunke and Zhang, 1999). The systematic differences between EVP and VP solvers, however, that lead to lower viscosities for EVP should be recognized and appreciated in climate modeling.

The case of the blocked channel is puzzling. On the one hand, it is the authors' opinion—that is not supported by any evidence so far—that the governing equations do not allow a total stoppage of the flow because the limited ice viscosity always allow some creep flow that will eventually break up any blocked channel or ice bridge. Thus one may speculate that the stoppage in the LSOR solutions emerge as a consequence of the numerics. On the other hand, experiments presented in this manuscript show that the actual viscosity in EVP solutions can be much lower due to the EVP-method of regularizing the momentum equations, so that EVP-solutions tend to have "weaker" ice. It is then plausible that this weaker ice can be pushed through a narrow channel more easily than "LSOR-ice". Note, that EVP-models have been shown to simulate stable ice bridges in other configurations and with different parameter choices (Dumont et al., 2009).

Most of the above effects are attributed to smaller viscosities in the EVP solutions. Hunke and Zhang (1999) observed a faster (and in that case more realistic) response of an EVP ice model than a VP model to fast changes in wind forcing. This faster response can also be explained by less rigid ice in the EVP solution. "Stronger" ice in VP-solvers such as LSOR or "weaker" ice in EVP could also be compensated for by different ice strength parameters (e.g. P^*) or parameterizations (e.g. Rothrock, 1975). For example, Lipscomb et al. (2007) mention that Rothrock's parameterization gives much higher ice strengths with their EVP ice model CICE than the parameterization by Hibler (1979) in Eq. (6), that is used here. This suggests that one needs to choose ice strength parameterizations in combination with other techniques, such as solving the momentum equations, to tune a sea-ice model to observations.

This paper leaves a number of open questions. At least in the quasi-steady state solutions of Section 4 we expected the EVP solutions to converge to VP solutions as $\partial/\partial t \to 0$. We can not explain why that is not the case and why the EVP solutions tend to have lower viscosities even in this case. Not only may the VP and EVP methods result in different solutions, but also the mere details of the numerical implementation, such as the use of a B- or C-grid, can change the solution, so that when the ice model reacts to forcing with blocking or arching, results can be completely different. Numerical simulations of sea-ice arching depend strongly on details of the rheology (Hibler et al., 2006, Dumont et al., 2009), but we found that the "effective" rheology is determined to some extent by numerics. Related to this are details such as lateral boundary conditions, which can affect the solutions to a considerable extent (e.g., Losch et al., 2010). The underlying causes for this troubling sensitivity to details of the numerics and geometry need be explored.

Acknowledgements. We thank Elizabeth Hunke for providing her original model configuration and for fruitful discussions, further Jean-François Lemieux for encouragement. We thank Malte Thoma, Rüdiger Gerdes, and Peter Lemke for helpful comments on earlier versions of the manuscript.

References

Balay, S., Gropp, W. D., McInnes, L. C., Smith, B. F., 2002. PETSc Users Manual. Tech. Rep. ANL-95/11 – Revision 2.1.3, Argonne National Laboratory.

Bouillon, S., Maqueda, M. Á. M., Legat, V., Fichefet, T., 2009. An elastic-viscous-plastic sea ice model formulated on Arakawa B and C grids. Ocean Modelling 27 (3–4), 174–184.

Danilov, S., Kivmann, G., Schröter, J., 2004. A finite element ocean model: Principles and evaluation. Ocean Modelling 6 (2), 125–150.

Dumont, D., Gratton, Y., Arbetter, T. E., 2009. Modeling the dynamics of the North Water Polynya ice bridge. J. Phys. Oceanogr. 39 (6), 1448–1461.

Fieg, K., Gerdes, R., Fahrbach, E., Beszczynska-Mller, A., Schauer, U., 2010. Simulation of oceanic volume transports through Fram Strait 1995-2005. Ocean Dynamics 60, 491–502.
URL http://dx.doi.org/10.1007/s10236-010-0263-9

Flato, G. M., Hibler, III, W. D., 1992. Modeling pack ice as a cavitating fluid. J. Phys. Oceanogr. 22 (6), 626–651.

Girard, L., Bouillon, S., Jérôme, W., Amitrano, D., Fichefet, T., Legat, V., 2011. A new modelling framework for sea ice models based on elasto-brittle rheology. Ann. Glaciol. 52 (57), 123–132.

Hibler, III, W. D., 1979. A dynamic thermodynamic sea ice model. J. Phys. Oceanogr. 9 (4), 815–846.

Hibler, III, W. D., Hutchings, J. K., Ip, C. F., 2006. Sea-ice arching and multiple flow states of Arctic pack ice. Ann. Glaciol. 44, 339–344.

Hibler, III, W. D., Ip, C. F., 1995. The effect of sea ice rheology on Arctic buoy drift. In: Dempsey, J. P., Rajapakse, Y. D. S. (Eds.), Ice Mechanics. Vol. 204 of AMD. Am. Soc. of Mech. Eng., New York, pp. 255–264.

Hundsdorfer, W., Trompert, R. A., 1994. Method of lines and direct discretization:

a comparison for linear advection. Applied Numerical Mathematics 13 (6), 469–490.

Hunke, E. C., 2001. Viscous-plastic sea ice dynamics with the EVP model: Linearization issues. J. Comp. Phys. 170, 18–38.

Hunke, E. C., Dukowicz, J. K., 1997. An elastic-viscous-plastic model for sea ice dynamics. J. Phys. Oceanogr. 27, 1849–1867.

Hunke, E. C., Dukowicz, J. K., 2002. The elastic-viscous-plastic sea ice dynamics model in general orthogonal curvilinear coordinates on a sphere—incorporation of metric terms. Mon. Weather Rev. 130 (7), 1847–1865.

Hunke, E. C., Zhang, Y., 1999. A comparison of sea ice dynamics models at high resolution. Mon. Weather Rev. 127, 396–408.

Hutchings, J. K., Jasak, H., Laxon, S. W., 2004. A strength implicit correction scheme for the viscous-plastic sea ice model. Ocean Modelling 7 (1–2), 111–133.

Kreyscher, M., Harder, M., Lemke, P., Flato, G. M., 2000. Results of the Sea Ice Model Intercomparison Project: Evaluation of sea ice reology schemes for use in climate simulations. J. Geophys. Res. 105 (C5), 11,299–11,320.

Lemieux, J.-F., Tremblay, B., 2009. Numerical convergence of viscous-plastic sea ice models. J. Geophys. Res. 114 (C05009).

Lemieux, J.-F., Tremblay, B., Sedláček, J., Tupper, P., Thomas, S., Huard, D., Auclair, J.-P., 2010. Improving the numerical convergence of viscous-plastic sea ice models with the Jacobian-free Netwon-Krylov method. J. Comp. Phys. 229, 280–2852.

Lemieux, J.-F., Tremblay, B., Thomas, S., Sedláček, J., Mysak, L. A., 2008. Using the preconditioned Generalized Minimum RESidual (GMRES) method to solve the sea-ice momentum equation. J. Geophys. Res. 113 (C10004).

Lipscomb, W. H., Hunke, E. C., Maslowski, W., Jakacki, J., 2007. Ridging, strength and stability in high-resolution sea ice models. J. Geophys. Res. 112 (C03S91).

Löhner, R., Morgan, K., Peraire, J., Vahdati, M., 1987. Finite element flux-corrected transport (FEM-FCT) for the Euler and Navier-Stokes equations. Int. J. Numer. Methods Fluids 7, 1093–1109.

Losch, M., Menemenlis, D., Campin, J.-M., Heimbach, P., Hill, C., 2010. On the formulation of sea-ice models. Part 1: Effects of different solver implementations and parameterizations. Ocean Modelling 33 (1–2), 129–144.

MITgcm Group, 2010. MITgcm User Manual. Online documentation, MIT/EAPS, Cambridge, MA 02139, USA, `http://mitgcm.org/public/r2_manual/latest/online_documents`.

Rothrock, D. A., 1975. The energetics of the plastic deformation of pack ice by ridging. J. Geophys. Res. 80 (33), 4514–4519.

Timmermann, R., Danilov, S., Schröter, J., Böning, C., Sidorenko, D., Rollenhagen, K., 2009. Ocean circulation and sea ice distribution in a finite element global sea ice – ocean model. Ocean Modelling 27 (3–4), 114–129.

Wilchinsky, A. V., Feltham, D. L., 2006. Modelling the rheology of sea ice as a collection of diamond-shaped floes. Journal of Non-Newtonian Fluid Mechanics 138, 22–32.

Wilchinsky, A. V., Feltham, D. L., Hopkins, M. A., 2010. Effect of shear rupture on aggregate scale formation in sea ice. J. Geophys. Res. 115 (C10002).

Zhang, J., Hibler, III, W. D., 1997. On an efficient numerical method for modeling sea ice dynamics. J. Geophys. Res. 102 (C4), 8691–8702.